Impact of local-field effects on the plasmonic enhancement of vibrational signals by infrared nanoantennas

Y. L. A. Rezus* **and O. Selig**

FOM Institute AMOLF, Science Park 104, 1098 XG Amsterdam, Netherlands

*rezus@amolf.nl

Abstract: We have developed an analytical model that provides a mechanistic description of the plasmonic enhancement of vibrational signals by infrared nanoantennas. Our treatment is based on a coupled-point-dipole model which considers the interaction between a point-like nanoantenna and a single vibrational dipole moment. This idealized model is refined in two consecutive steps. The first step generalizes the model to make the treatment of non-point-like nanoantennas possible. The second step deals with local-field effects originating from the mutual interaction of the molecular vibrations. We have compared the results of our model with finite-difference time-domain simulations, and we find that our model predicts both the lineshapes and the amplitudes of the vibrational signals in a quantitative manner. Our analysis shows that the local-field effects play a surprisingly dominant role in the plasmonic enhancement, and we discuss possibilities of engineering this local field in order to further boost the plasmonic amplification.

OCIS codes: (300.6340) Spectroscopy: Spectroscopy, infrared; (240.6680) Optics at surfaces: Surface plasmons; (250.5403) Optoelectronics: Plasmonics.

References and links

1. A. Hartstein, J. R. Kirtley, and J. C. Tsang, "Enhancement of the infrared absorption from molecular monolayers with thin metal overlayers," Phys. Rev. Lett. **45**, 201–204 (1980).
2. M. Osawa, "Dynamic processes in electrochemical reactions studied by surface-enhanced infrared absorption spectroscopy (SEIRAS)," Bull. Chem. Soc. Jpn. **70**, 2861–2880 (1997).
3. A. E. Bjerke, P. R. Griffiths, and W. Theiss, "Surface-enhanced infrared absorption of Co on platinized platinum," Anal. Chem. **71**, 1967–1974 (1999).
4. E. Johnson and R. Aroca, "Surface-enhanced infrared-spectroscopy of monolayers," J. Phys. Chem. **99**, 9325–9330 (1995).
5. M. Osawa and M. Ikeda, "Surface-enhanced infrared-absorption of para-nitrobenzoic acid deposited on silver island films - contributions of electromagnetic and chemical mechanisms," J. Phys. Chem. **95**, 9914–9919 (1991).
6. D. Enders and A. Pucci, "Surface enhanced infrared absorption of octadecanethiol on wet-chemically prepared Au nanoparticle films," Appl. Phys. Lett. **88**, 184104 (2006).
7. R. Adato, A. A. Yanik, J. J. Amsden, D. L. Kaplan, F. G. Omenetto, M. K. Hong, S. Erramilli, and H. Altug, "Ultra-sensitive vibrational spectroscopy of protein monolayers with plasmonic nanoantenna arrays," Proc. Natl. Acad. Sci. USA **106**, 19227–19232 (2009).
8. F. Neubrech, A. Pucci, T. W. Cornelius, S. Karim, A. García-Etxarri, and J. Aizpurua, "Resonant plasmonic and vibrational coupling in a tailored nanoantenna for infrared detection," Phys. Rev. Lett. **101**, 157403 (2008).
9. S. Bagheri, K. Weber, T. Gissibl, T. Weiss, F. Neubrech, and H. Giessen, "Fabrication of square-centimeter plasmonic nanoantenna arrays by femtosecond direct laser writing lithography: effects of collective excitations on seira enhancement," ACS Photonics **2**, 779–786 (2015).

#262910 Received 8 Apr 2016; revised 24 May 2016; accepted 24 May 2016; published 26 May 2016

10. H. Aouani, H. Sipova, M. Rahmani, M. Navarro-Cia, K. Hegnerova, J. Homola, M. Hong, and S. A. Maier, "Ultrasensitive broadband probing of molecular vibrational modes with multifrequency optical antennas," ACS Nano **7**, 669–675 (2013).
11. L. V. Brown, K. Zhao, N. King, H. Sobhani, P. Nordlander, and N. J. Halas, "Surface-enhanced infrared absorption using individual cross antennas tailored to chemical moieties," J. Am. Chem. Soc. **135**, 3688–3695 (2013).
12. L. V. Brown, X. Yang, K. Zhao, B. Y. Zheng, P. Nordlander, and N. J. Halas, "Fan-shaped gold nanoantennas above reflective substrates for surface-enhanced infrared absorption (seira)," Nano Lett. **15**, 1272–1280 (2015).
13. D. Dregely, F. Neubrech, H. Duan, R. Vogelgesang, and H. Giessen, "Vibrational near-field mapping of planar and buried three-dimensional plasmonic nanostructures," Nat. Commum. **4**, 2237 (2013).
14. J. M. Hoffmann, X. H. Yin, J. Richter, A. Hartung, T. W. W. Mass, and T. Taubner, "Low-cost infrared resonant structures for surface-enhanced infrared absorption spectroscopy in the fingerprint region from 3 to 13 μm," J. Phys. Chem. C **117**, 11311–11316 (2013).
15. D. Rodrigo, O. Limaj, D. Janner, D. Etezadi, F. Javier Garcia de Abajo, V. Pruneri, and H. Altug, "Mid-infrared plasmonic biosensing with graphene," Science **349**, 165–168 (2015).
16. M. Abb, Y. D. Wang, N. Papasimakis, C. H. de Groot, and O. L. Muskens, "Surface-enhanced infrared spectroscopy using metal oxide plasmonic antenna arrays," Nano Lett. **14**, 346–352 (2014).
17. F. Neubrech, S. Beck, T. Glaser, M. Hentschel, H. Giessen, and A. Pucci, "Spatial extent of plasmonic enhancement of vibrational signals in the infrared," ACS Nano **8**, 6250–6258 (2014).
18. S. Gottheim, H. Zhang, A. O. Govorov, and N. J. Halas, "Fractal nanoparticle plasmonics: the cayley tree," ACS Nano **9**, 3284–3292 (2015).
19. K. Chen, R. Adato, and H. Altug, "Dual-band perfect absorber for multispectral plasmon-enhanced infrared spectroscopy," ACS Nano **6**, 7998–8006 (2012).
20. O. Selig, R. Siffels, and Y. L. A. Rezus, "Ultrasensitive ultrafast vibrational spectroscopy employing the near field of gold nanoantennas," Phys. Rev. Lett. **114**, 233004 (2015).
21. L. Novotny, "Effective wavelength scaling for optical antennas," Phys. Rev. Lett. **98**, 266802 (2007).
22. H. J. Chen, L. Shao, K. C. Woo, J. F. Wang, and H. Q. Lin, "Plasmonic-molecular resonance coupling: plasmonic splitting versus energy transfer," J. Phys. Chem. C **116**, 14088–14095 (2012).
23. C. F. Bohren and D. R. Huffman, *Absorption and Scattering of Light by Small Particles* (Wiley-VCH Verlag, 2004).
24. E. M. Purcell and C. R. Pennypacker, "Scattering and absorption of light by nonspherical dielectric grains," Astrophys. J. **186**, 705–714 (1973).
25. B. T. Draine and P. J. Flatau, "Discrete-dipole approximation for scattering calculations," J. Opt. Soc. Am. A **11**, 1491–1499 (1994).
26. L. Novotny and B. Hecht, *Principles of Nano-Optics* (Cambridge University, 2006).
27. T. Neuman, P. Alonso-Gonzalez, A. Garcia-Etxarri, M. Schnell, R. Hillenbrand, and J. Aizpurua, "Mapping the near fields of plasmonic nanoantennas by scattering-type scanning near-field optical microscopy," Laser Photonics Rev. **9**, 637–649 (2015).
28. P. Alonso-Gonzalez, P. Albella, F. Neubrech, C. Huck, J. Chen, F. Golmar, F. Casanova, L. E. Hueso, A. Pucci, J. Aizpurua, and R. Hillenbrand, "Experimental verification of the spectral shift between near- and far-field peak intensities of plasmonic infrared nanoantennas," Phys. Rev. Lett. **110**, 203902 (2013).
29. A. M. Kern and O. J. F. Martin, "Excitation and reemission of molecules near realistic plasmonic nanostructures," Nano Lett. **11**, 482–487 (2011).
30. J. D. Jackson, *Classical Electrodynamics* (John Wiley and Sons, Inc., 1999).
31. A. Soldera and E. Monterrat, "Mid-infrared optical properties of a polymer film: comparison between classical molecular simulations, spectrometry, and ellipsometry techniques," Polymer **43**, 6027–6035 (2002).
32. E. D. Palik, *Handbook of Optical Constants of Solids* (Academic, 1985).

1. Introduction

Infrared spectroscopy is a well-known analytical tool that is widely used to identify molecular species. The technique owes its chemical specificity to the fact molecules leave their 'vibrational fingerprint' in the infrared spectrum. That is, the chemical groups inside molecules possess characteristic vibrational frequencies which give rise to sharp infrared absorption bands. Unfortunately, despite its exquisite chemical specificity, infrared spectroscopy is a relatively insensitive technique requiring large quantities of material. This poor sensitivity is a consequence of the weak absorption cross sections of molecular vibrations, which are typically a thousand times smaller compared to the cross sections of electronic transitions. The sensitivity problem of infrared spectroscopy is partly overcome in a variant of the method

#262910 Received 8 Apr 2016; revised 24 May 2016; accepted 24 May 2016; published 26 May 2016

known as surface-enhanced infrared absorption (SEIRA) spectroscopy [1–6]. In this technique chemically roughened metal films are employed onto which the molecules of interest are adsorbed. The excitation of plasmonic modes inside the metal film leads to strong near fields which couple to the molecular vibrations and enhance the spectroscopic signals. However, in conventional SEIRA spectroscopy the spectral overlap between the broad plasmonic modes and the sharp molecular vibrations is far from optimal, so that in practice the signal enhancement remains modest.

In recent years the SEIRA technique has undergone a revival with the substitution of the metal films for tailored (metallic or non-metallic) nanostructures [7–17], fabricated using lithographic means. These nanostructures, which we will generically refer to as infrared nanoantennas, exhibit a resonance in the mid-infrared that can be tuned to a molecular vibration of interest. The resonant character of the plasmonic excitation in these structures leads to much larger field enhancements compared to metallic films and thereby to comparatively larger signal enhancements. To date a variety of IR nanoantennas have been explored for the ultrasensitive detection of molecules, among which figure coupled arrays of nanoantennas [7], various nanoclusters, fractal-shaped antennas [10,18] and perfect absorber structures [19]. Very recently we have shown that it is possible to use the intense near fields of infrared nanoantennas to move beyond the conventional linear spectroscopic detection of molecules and to even perform advanced nonlinear spectroscopic experiments on the detected molecules [20]. In the future this extension of the SEIRA technique will allow one to study dynamic processes, such as chemical reactions or energy transfer processes within or between the detected molecules.

An important aspect of infrared nanoantennas is the fact that the amplified vibrational signals do not necessarily give rise to the familiar absorptive lineshapes known from conventional infrared spectroscopy. Instead the nanoantenna-enhanced vibrational resonances often have a dispersive character, so that they appear distorted. These lineshape distortions are not a serious problem if one simply considers nanoantenna-SEIRA as an ultrasensitive *detection* technique. However, from the *spectroscopic* perspective these distortions are more problematic. In molecular spectroscopy one typically relies on the widths, amplitudes, spectral shifts and detailed shapes of the vibrational bands to deduce information about molecular structures and dynamics. Therefore for spectroscopic applications—both linear and nonlinear—it is important to understand how the metal nanostructures affect the vibrational lineshape, so that one can distinguish between lineshape features that contain molecular information and lineshape features that are merely a consequence of the amplification process. In the literature finite element electromagnetic simulations are commonly used to predict the vibrational lineshapes observed in nanoantenna-SEIRA [8]. While these methods can accurately predict the lineshapes observed, they do not provide intuitive understanding of the underlying physical mechanisms. In this work we aim to develop such intuitive understanding by constructing an analytic model of the coupling between molecular vibrations and infrared nanoantennas. This model will provide insight into the factors that govern the degree of signal enhancement, as well as how these factors affect the observed lineshapes.

Our approach consists of three steps. We start out with a highly idealized model in which we consider only two point dipoles. The first point dipole represents the nanoantenna while the second point dipole represents all the molecular vibrations interacting with the nanoantenna. This model can be solved analytically, and we show that despite its simplicity the model already describes many features of the amplification process in a qualitative manner. In the second step we refine the model in such a way that it becomes applicable to realistic nanoantenna geometries (as opposed to a point-like nanoantenna). The model now allows one to quantitatively compute the response of a nanoantenna covered by a thin layer of dielectric material, as long as this material is described by either a purely resonant or by a purely non-resonant permittivity. It

#262910 Received 8 Apr 2016; revised 24 May 2016; accepted 24 May 2016; published 26 May 2016

turns out that the model, at this stage, breaks down for materials that have both a resonant and a non-resonant permittivity. In the third step we show that this breakdown is due to the neglect of local-field effects, and we finish by incorporating these effects into the model. The resulting model allows one to accurately compute the plasmonic enhancement factor for a particular vibrational band, and, moreover, it identifies the different physical contributions to this enhancement factor. A major result of the present work is the finding that for most molecular vibrations the local molecular field, which was mostly overlooked in the past, plays a surprisingly large role in the plasmonic enhancement mechanism.

2. Results and discussion

Figure 1 illustrates the principles underlying the use of infrared nanoantennas. Typically an array of such nanoantennas is fabricated on top of an infrared-transparent substrate, such as CaF_2, and the material to be detected is deposited as a thin layer on top of the nanoantennas (Fig. 1(a)). In this work we focus on rod-like nanoantennas because their resonance frequency can easily be tuned to the mid-infrared. We have computed the (extinction) cross-section spectra of three isolated gold nanoantennas of different length using finite-difference time-domain (FDTD) simulations (Fig. 1(b)). For light polarized along the long antenna axis the nanoantennas display a plasmon resonance in the mid-infrared, which shifts to lower frequencies with increasing nanoantenna length [8,21]. The nanoantenna spectrum is extremely sensitive to the material in its direct environment, which makes the nanoantennas ideal for sensing applications. This point is illustrated in Fig. 1(c), which shows that covering the nanoantenna by a 10 nm layer of dielectric material with an index of refraction of 1.48 leads to a significant redshift of the spectrum. Next we consider the effect of covering the nanoantenna by a material that exhibits a vibrational resonance. As a prototypical example of such a material we have chosen the molecular polymer polymethylmetacrylate (PMMA) because it is often used in experimental studies due to its ease of spincoating [14, 22]. PMMA displays a sharp vibrational resonance at 1730 cm^{-1} which results from its C=O stretching vibration. It can be seen that the spectrum of the C=O vibration shows up as an absorptive dip on top of the nanoantenna spectrum (Fig. 1(d)). In order to highlight the amplified vibrational spectrum we subtract the bare nanoantenna spectrum from the spectrum of the coated nanoantenna as is illustrated in Fig. 1(e). This figure also shows the amplified vibrational spectrum for nanoantennas of different lengths. It can be seen that, depending on the detuning between the nanoantenna and the vibrational resonance, a variety of lineshapes can be observed, from absorptive to dispersive as well as any shape in between. In the following we develop an analytical model, along the lines described in the introduction, that can quantitatively explain the spectral effects illustrated in Fig. 1.

#262910 Received 8 Apr 2016; revised 24 May 2016; accepted 24 May 2016; published 26 May 2016

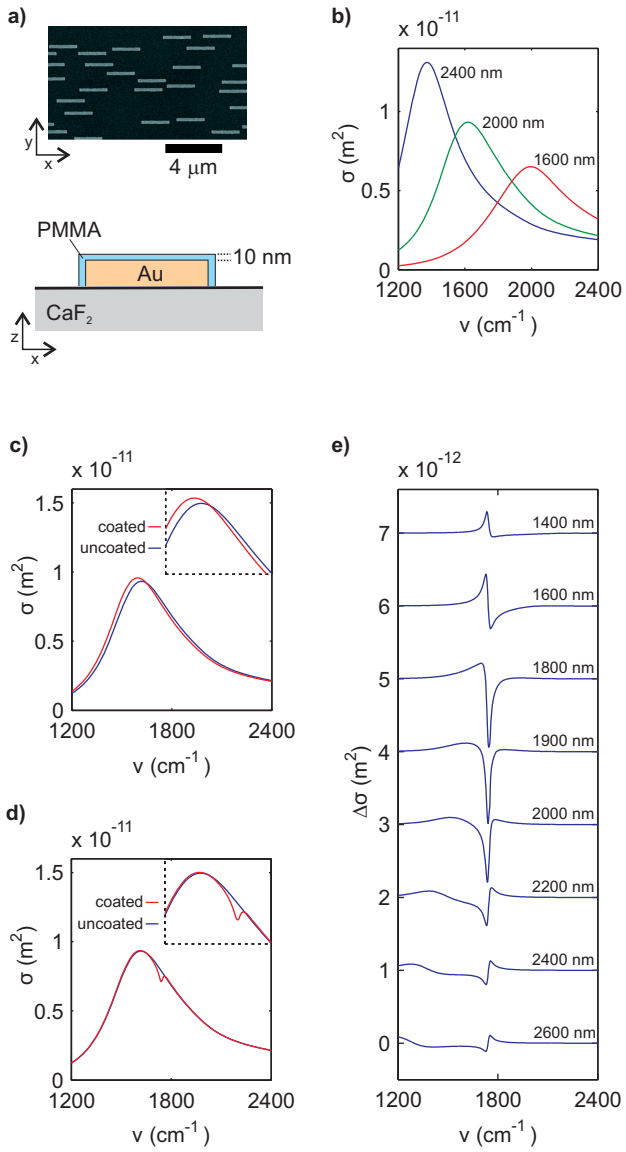

Fig. 1. (a, top) Scanning electron microscope image of an array of gold nanoantennas fabricated on top of a CaF_2 substrate. (a, bottom) Geometry used in the FDTD simulations to calculate the cross section of an isolated nanoantenna and its modification due to the presence of a shell of dielectric material. (b) Simulated extinction cross sections of gold nanoantennas on top of CaF_2. The nanoantennas have a width of 200 nm, a height of 100 nm and a varying length (1600 nm, 2000 nm and 2400 nm). (c) Cross-section spectrum of a 2000 nm nanoantenna (blue line) and of the same nanoantenna coated with a 10 nm layer of dielectric material characterized by an index of refraction of 1.48 (red line). The inset shows a zoom around the cross section maximum. (d) Cross-section spectrum of a 2000 nm nanoantenna (blue line) and of the same nanoantenna coated with a 10 nm layer of PMMA. The PMMA is modeled using a Lorentzian absorption at 1730 cm^{-1} and a background refractive index of 1. (e) Effect of the nanoantenna length on the amplified vibrational lineshape. The curves are calculated by subtracting the spectrum of a bare nanoantenna from the spectrum of a coated nanoantenna. For clarity the different curves are shifted vertically by 10^{-12} m^2.

#262910 Received 8 Apr 2016; revised 24 May 2016; accepted 24 May 2016; published 26 May 2016

2.1. Step 1: point-dipole model

We start by describing the interaction between a nanoantenna and the molecules that cover it using a simple coupled-dipole model. In this model we only consider two point dipoles: the first point dipole (p_{ant}) represents the nanonantenna while the second point dipole (p_{vib}) represents all molecular vibrations lumped together. The nanoantenna is characterized by the frequency-dependent polarizability $\alpha_{\text{ant}}(\omega)$ and the vibrational dipole moment by the frequency-dependent polarizability $\alpha_{\text{vib}}(\omega)$. To avoid clutter we will drop the explicit frequency dependence henceforward. For the moment we treat the case of free-space coupling between the two point dipoles, and we will discuss the effect of the substrate at the end of this section.

Our experimental observable is the extinction cross section σ_{ant} of the nanoantenna and its modification $\Delta\sigma$ due to the presence of the vibrational dipole. In general the extinction cross section σ of a dipolar particle is related to the imaginary part of its polarizability [23]

$$\sigma = \frac{2\pi}{\lambda\varepsilon_0}\text{Im}[\alpha] \tag{1}$$

Here ε_0 is the permittivity of free space, and λ is the free-space wavelength. For the treatment to come it is useful to briefly recall the origin of this expression, which can be done by considering the definition of the extinction cross section

$$\sigma = \frac{P_{\text{inc}}}{I_{\text{inc}}} \tag{2}$$

where P_{inc} is the work (per unit time) done on the particle by the incident field and I_{inc} is the incident intensity. By substituting the standard expressions $I_{\text{inc}} = \frac{1}{2}\varepsilon_0 c|E_0|^2$ and

$$P_{\text{inc}} = \frac{1}{2}\omega\text{Im}[pE_0^*], \tag{3}$$

with p the complex amplitude of the induced dipole moment of the particle and E_0 the complex amplitude of the incoming electric field (we have assumed that all fields vary as $\sim \exp[-i\omega t]$) one directly obtains Eq. (1).

Let us now consider the coupling of p_{ant} and p_{vib}. Both dipoles experience two fields: the incident field and the field originating from the other particle. This leads to the coupled-dipole equations [24, 25]

$$p_{\text{ant}} = \alpha_{\text{ant}}E_0 + \alpha_{\text{ant}}G(r_{\text{ant}}, r_{\text{vib}})p_{\text{vib}} \tag{4}$$

$$p_{\text{vib}} = \alpha_{\text{vib}}E_0 + \alpha_{\text{vib}}G(r_{\text{vib}}, r_{\text{ant}})p_{\text{ant}} \tag{5}$$

Here $G(r_1, r_2)$ is the Green's function for a dipole located at r_2. We should point out that for simplicity we have adopted a scalar description. By solving for the dipole moments we see that the effect of the coupling is to modify the polarizabilities of the two dipoles into new, effective polarizabilities

$$p_{\text{ant}} = \alpha_{\text{eff,ant}}E_0 = \frac{\alpha_{\text{ant}} + \alpha_{\text{ant}}\alpha_{\text{vib}}G}{1 - \alpha_{\text{ant}}\alpha_{\text{vib}}G^2}E_0 \tag{6}$$

$$p_{\text{vib}} = \alpha_{\text{eff,vib}}E_0 = \frac{\alpha_{\text{vib}} + \alpha_{\text{ant}}\alpha_{\text{vib}}G}{1 - \alpha_{\text{ant}}\alpha_{\text{vib}}G^2}E_0 \tag{7}$$

Here we have used the reciprocity theorem to equate the two Green's functions and simply denoted them as G [26]. In our experiments we typically measure the absorption difference

#262910 Received 8 Apr 2016; revised 24 May 2016; accepted 24 May 2016; published 26 May 2016

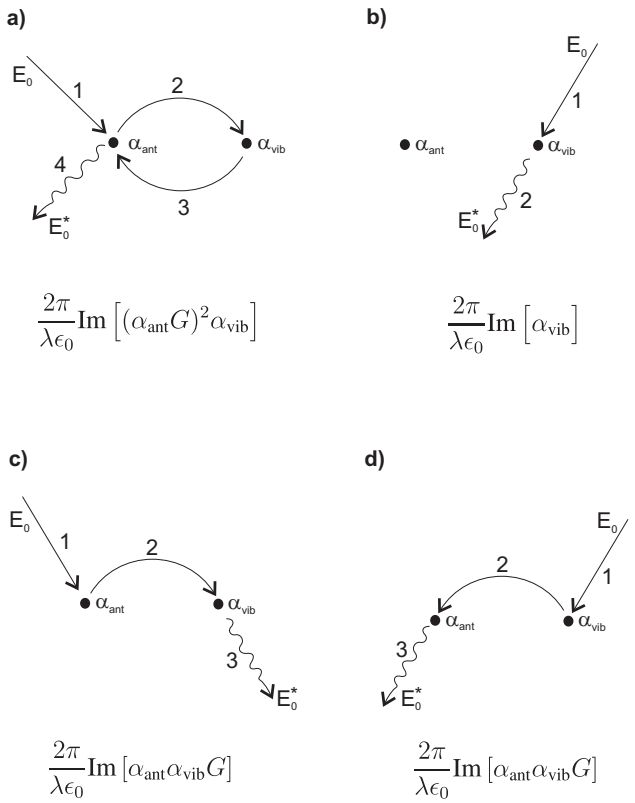

Fig. 2. Scattering diagrams representing the different terms in the expansion from Eq. (9). (a) Diagram representing the leading term in the expansion ($n = 1$ in the first summation symbol). (b) Diagram representing the leading term ($n = 0$) of the second summation symbol. This interaction process represents the direct interaction of the light with the vibrational dipole. (c,d) Scattering diagrams that are grouped together under the third summation symbol of Eq. (9).

of the coated and the uncoated nanoantennas, so that we have the following experimental observable

$$\Delta\sigma = \frac{2\pi}{\lambda\varepsilon_0}\mathrm{Im}\left[\alpha_{\mathrm{eff,ant}} + \alpha_{\mathrm{eff,vib}} - \alpha_{\mathrm{ant}}\right] \tag{8}$$

While Eq. (8) provides an exact analytical expression for the cross-section change of the nanoantenna, it turns out to be useful to expand the solution in a geometric series

$$\Delta\sigma = \frac{2\pi}{\lambda\varepsilon_0}\mathrm{Im}\left\{\sum_{n=1}^{\infty}\alpha_{\mathrm{ant}}^{n+1}\alpha_{\mathrm{vib}}^{n}G^{2n} + \sum_{n=0}^{\infty}\alpha_{\mathrm{ant}}^{n}\alpha_{\mathrm{vib}}^{n+1}G^{2n} + 2\sum_{n=0}^{\infty}\alpha_{\mathrm{ant}}^{n+1}\alpha_{\mathrm{vib}}^{n+1}G^{2n+1}\right\} \tag{9}$$

The expansion above allows one to view the amplification mechanism as a multiple-scattering problem, which is a useful approach that has, for example, also been followed to describe the signals in near-field scanning optical microscopy [27]. The terms in the expansion can be interpreted as different interaction processes between the two point dipoles. We will represent these interaction processes symbolically using scattering diagrams as those illustrated in Fig. 2. In the following we will briefly illustrate how to read these diagrams. The diagram in Fig. 2(a)

#262910 Received 8 Apr 2016; revised 24 May 2016; accepted 24 May 2016; published 26 May 2016

represents the leading term in the expansion ($n = 1$ term in the first summation symbol). In this diagram the incident arrow (1) represents the incident field E_0 which polarizes the antenna. As a result the antenna generates an enhanced near field which polarizes the vibrational dipole (2). In turn, the vibrational dipole acts back and generates a field at the location of the antenna, which modifies the antenna polarization (3). Finally we compute the work done by the incident field on this part of the antenna polarization (4). This last process is represented by the wiggly arrow. Below the diagram we have written the contribution to the cross-section change due to this interaction process. Inspection of Fig. 2 makes it clear that there are three types of scattering diagrams, each type corresponding to one of the three summation symbols in Eq. (9). The first summation symbol groups together the diagrams that start and end on the nanoantenna, an example of which is the diagram that we just discussed (Fig. 2(a)). The second summation symbol corresponds to diagrams that start and end on the vibrational dipole (see, for example, Fig. 2(b)). Finally the third summation symbol contains diagrams that start on one dipole and end on the other dipole. The diagram in Fig. 2(c) is an example of this third type of scattering diagram. Here the incident field polarizes the vibrational dipole (1). Next the vibrational dipole polarizes the nanoantenna (2). Finally we compute the work done on the nanoantenna (3). We note that the factor of 2 in front of the third summation symbol (Eq. (9)) comes from the fact that this summation symbol groups together two types of diagrams (i.e. diagrams starting on the nanoantenna and ending on the vibration and vice versa), which contribute equally to the total cross-section change.

Replacing Eq. (9) by the leading term in its expansion we obtain the following approximation for the cross-section change

$$\Delta\sigma = \frac{2\pi}{\lambda\varepsilon_0}\mathrm{Im}\left[(\alpha_{\mathrm{ant}}G)^2\alpha_{\mathrm{vib}}\right] \tag{10}$$

Interestingly, although Eq. (10) is based on a highly idealized model, this expression can already qualitatively explain many of the features observed in Fig. 1. Equation (10) shows that the nanoantenna amplifies the original vibrational spectrum by the complex-valued factor $(\alpha_{\mathrm{ant}}G)^2$, which represents the square of the field enhancement. Due to the complex nature of the amplification factor the (enhanced) vibrational signal $\Delta\sigma$ typically contains both an absorptive ($\mathrm{Im}[\alpha_{\mathrm{vib}}]$) and a dispersive component ($\mathrm{Re}[\alpha_{\mathrm{vib}}]$). It is straightforward to see that there are three circumstances under which purely absorptive lineshapes are observed: if the antenna is driven on resonance, far below resonance or far above resonance. In the first case there is a $\pi/2$ phase lag between the incident electric field and the antenna polarization: this leads to a negative value of the amplification factor $(\alpha_{\mathrm{ant}}G)^2$, so that the vibrational signal is observed as an absorption *dip* on top of the antenna resonance. Driving the antenna far below resonance or far above resonance results in phase shifts of 0 and π, respectively, so that in these two circumstances absorptive *peaks* are observed. It is useful to point out that it is the backaction of the vibrational dipole on the nanoantenna which is responsible for the amplification of the vibrational spectrum (as also becomes apparent from the scattering diagram in Fig. 2(a)). Intuitively one might have expected the amplification to be a consequence of the (far-field) radiation emitted by the vibrational dipole after its excitation by the strong near field of the nanoantenna. This process does in fact contribute to the amplification process (it corresponds to the scattering diagram depicted in Fig. 2(c)). Its contribution is, however, relatively small because its amplitude scales only linearly with the field enhancement $\alpha_{\mathrm{ant}}G$, which should be compared to the quadratic scaling of the backaction process (Fig. 2(a)). Moreover, it is interesting to note that the scattering diagram in Fig. 2(c) leads to dispersive lineshapes for a vibration that is in perfect resonance with a nanoantenna, in contrast to the inverted absorptive shapes which are observed in experiments and simulations [20, 28].

Before continuing, it is useful to roughly estimate the accuracy of the approximation at the

#262910 Received 8 Apr 2016; revised 24 May 2016; accepted 24 May 2016; published 26 May 2016

origin of Eq. (10). We readily see that compared to the leading scattering diagram (Fig. 2(a)) the contributions of the scattering diagrams in Fig. 2(b) and Figs. 2(c) and 2(d) are smaller by a factor of $(\alpha_{\text{ant}}G)^2$ and $(\alpha_{\text{ant}}G)$, respectively. Using the fact that $\alpha_{\text{ant}}G$ represents the field enhancement of the antenna at the location of the vibrational dipole, we can get a numerical estimate of these factors from FDTD simulations of bare nanoantennas (Fig. 1(b)). It turns out that the average nanoantenna field enhancement experienced by the shell of PMMA is approximately 10. From this value we conclude that, compared to the leading scattering diagram, the contribution of the diagram in Fig. 2(b) is smaller by two orders of magnitude while those in Fig. 2(c)-(d) are smaller by one order of magnitude. Next we consider the scaling behavior of the consecutive scattering diagrams grouped together under the first summation symbol in Eq. (9). These scale by the factor $\alpha_{\text{ant}}\alpha_{\text{vib}}G^2$. In order to estimate this factor we again turn to the FDTD simulations. The cross section of a nanoantenna is approximately 10^{-11} m^2. On the other hand from the known transmission (98.9 %) of a 10 nm film of PMMA we estimate the cross section of the PMMA shell to be 10^{-14} m^2. From the ratio of these cross sections combined with the nanoantenna field enhancement ($\alpha_{\text{ant}}G \sim 10$) we find that $\alpha_{\text{ant}}\alpha_{\text{vib}}G^2 \sim 10^{-1}$. We conclude that the largest correction terms to the cross-section change (Eq. (10)) are approximately one order of magnitude smaller than the leading term.

We conclude this section by discussing the effect of the substrate. In principle, all expressions can remain unmodified if (whenever a substrate is present) we simply consider α_{ant} and G as functions that are renormalized to contain the effect of the interface in them. There is, however, a subtlety which has to do with the Fresnel reflection of the interface and the fact that our cross sections are defined with respect to the *incident* electric field (as opposed to the local electric field). Due to the reflection, the electric field experienced by our point dipoles is attenuated relative to the incident field by the factor $(1-r)$ where $r = (n_s - 1)/(n_s + 1)$ is the Fresnel reflection coefficient and n_s the refractive index of the substrate. Because the incident intensity, however, is still given by $I_{\text{inc}} = 1/2c\varepsilon_0|E_0|^2$, this results in the scaling of all expressions by the factor $(1-r)^2$. The expression for the cross-section change of a nanoantenna on a surface becomes

$$\Delta\sigma = \frac{2\pi S_{\text{sub}}}{\lambda\varepsilon_0}\text{Im}\left[(\alpha_{\text{ant}}G)^2\alpha_{\text{vib}}\right] \tag{11}$$

where we defined the substrate scaling factor

$$S_{\text{sub}} = \frac{4}{(1+n_s)^2} \tag{12}$$

It can be seen that due to the interference between the incoming and the reflected field at the dielectric interface the refractive index of the substrate has quite an influence on the degree of vibrational amplification. For instance, even if we design two nanoantennas to have the same field enhancement ($\alpha_{\text{ant}}G$) on silicon ($n = 3.42$) and on calcium fluoride ($n = 1.42$), the amplification factor will still be 70% smaller in the case of silicon compared to calcium fluoride.

2.2. Step 2: finite antenna size

Equation (11) has given us an intuitive picture of the mechanism underlying the vibrational amplification process. Unfortunately, one cannot use this expression to quantitatively evaluate the amplified vibrational spectrum in the case of a realistic nanoantenna (i.e. a nanoantenna that cannot be described as a point dipole). The main issue lies in the backaction process (step 3 in Fig. 2(a)). Here we had implicitly assumed that the dipole moment induced in the nanoantenna by the vibrational dipole is $\Delta p_{\text{ant}} = \alpha_{\text{ant}}G(r_{\text{ant}}, r_{\text{vib}})p_{\text{vib}}$. However, this expression obviously breaks down for a finite-sized nanoantenna because it is not clear at what location r_{ant} the Green's function should be evaluated. The aim of this section is to rewrite Eq. (11) in such a

#262910 Received 8 Apr 2016; revised 24 May 2016; accepted 24 May 2016; published 26 May 2016

way that it provides a quantitative description of the interaction of a finite-sized nanoantenna with a collection of point-like vibrational dipoles.

Before we start, let us generalize Eq. (11) to take into account the tensorial nature of α_{ant} and G. For the moment we still assume point dipoles. We assume that the polarizability tensor of the nanoantenna is diagonal in the coordinate system of Fig. 1(a) (with diagonal elements $\alpha_{\text{ant,x}}$, $\alpha_{\text{ant,y}}$ and $\alpha_{\text{ant,z}}$). For the vibrational dipole we assume an isotropic polarizability α_{vib} to account for the isotropic distribution of the transition dipole moments of the vibrations. It is straightforward to show that, for an incident field $E_x^{(0)}$ polarized along the long antenna axis, Eq. (11) generalizes to the following expression.

$$\Delta\sigma = \frac{2\pi S_{\text{sub}}}{\lambda\varepsilon_0}\text{Im}\left[\alpha_{\text{ant,x}}^2(G_{xx}^2+G_{yx}^2+G_{zx}^2)\alpha_{\text{vib}}\right] \tag{13}$$

In writing Eq. (13) we used the general form of the reciprocity relation [26]

$$G_{\alpha\beta}(r_1,r_2) = G_{\beta\alpha}(r_2,r_1) \tag{14}$$

As a next step we rewrite Eq. (13) in a way which does not make reference to the Green's function. To this end, it is useful to recall that the scattering diagram in Fig. 2(a) describes two processes. Firstly, the enhancement of the incident field E_0 by the nanoantenna, and secondly the amplification of the vibrational dipole moment p_{vib} by the nanoantenna. In order to describe these two amplification processes we introduce two tensorial quantities: the field-enhancement tensor $f_{\alpha\beta}$ and the dipole-amplification tensor $f'_{\alpha\beta}$. We define the field-enhancement tensor as

$$f_{\alpha\beta} = \frac{E_\alpha(r_{\text{vib}})}{E_\beta^{(0)}(r_{\text{vib}})} \tag{15}$$

where $E_\beta^{(0)}(r_{\text{vib}})$ is the field at the location of the vibrational dipole in the absence of the nanoantenna, and $E_\alpha(r_{\text{vib}})$ is the same field in the presence of the nanoantenna. This definition assumes that the incident field points in the direction of one of the cartesian axes. We further remark that the field-enhancement tensor depends on the type of illumination used, which we consider here to be plane-wave illumination at normal incidence. In terms of the field-enhancement tensor we can express the induced vibrational dipole moment $\Delta\vec{p}_{\text{vib}}$ (i.e. steps 1 and 2 in Fig. 2(a)) as

$$\Delta\vec{p}_{\text{vib}} = \alpha_{\text{vib}}\begin{pmatrix} f_{xx}-1 \\ f_{yx} \\ f_{zx}\end{pmatrix}E_x^{(0)}(r_{\text{vib}}) \tag{16}$$

Here we point out that the different form of $\Delta p_{\text{vib,x}}$ is due to the fact that the scattering diagram in Fig. 2(a) does not include the direct polarization of the vibrational dipole by the incident field. Next we introduce the dipole amplification tensor $f'_{\alpha\beta}$, which describes the factor by which a vibrational dipole (that is aligned with one of the cartesian axes) is amplified by the nanoantenna.

$$f'_{\alpha\beta} = \frac{p_{\text{tot},\alpha}}{p_{\text{vib},\beta}} \tag{17}$$

Here we have defined $f'_{\alpha\beta}$ in such a way that it corresponds to the factor by which the dipole moment $p_{\text{tot},\alpha}$ of the whole assembly (i.e. vibrational dipole plus nanoantenna) is amplified compared to the situation in which there is only a vibrational dipole. For our analysis we will only need the following three elements

$$f'_{xx} = \frac{\Delta p_{\text{ant,x}}}{p_{\text{vib,x}}}+1, \qquad f'_{xy} = \frac{\Delta p_{\text{ant,x}}}{p_{\text{vib,y}}}, \qquad f'_{xz} = \frac{\Delta p_{\text{ant,x}}}{p_{\text{vib,z}}} \tag{18}$$

#262910 Received 8 Apr 2016; revised 24 May 2016; accepted 24 May 2016; published 26 May 2016

where $\Delta p_{\text{ant,x}}$ is the induced dipole moment in the nanoantenna. In terms of the tensors $f_{\alpha\beta}$ and $f'_{\alpha\beta}$ Eq. (13) reads as follows

$$\Delta\sigma = \frac{2\pi S_{\text{sub}}}{\lambda\,\varepsilon_0}\,\text{Im}\left[\left((f_{xx}-1)(f'_{xx}-1)+f_{yx}f'_{xy}+f_{zx}f'_{xz}\right)\alpha_{\text{vib}}\right] \tag{19}$$

The obvious question arises whether it is possible to relate the dipole amplification tensor $f'_{\alpha\beta}$ to the field enhancement tensor $f_{\alpha\beta}$ (given that the field enhancement can easily be obtained from FDTD simulations). In the next section we will show that this is indeed possible using electromagnetic reciprocity [26, 29].

2.2.1. Relationship between the field enhancement and the dipole amplification

In this section we aim to express the dipole amplification tensor elements $f'_{x\beta}$ in terms of the field enhancement tensor elements $f_{\beta x}$. We will compute the elements f'_{xx}, f'_{xy} and f'_{xz} by explicitly considering the source generating the plane wave that excites the nanoantenna. This source will be a point dipole located far away from the nanoantenna (so that the nanoantenna is effectively excited by a plane wave at normal incidence). This procedure will allow us to write the tensor elements $f_{\alpha\beta}$ and $f'_{\alpha\beta}$ as a ratio of Green's functions. It turns out that this calculation needs to be performed separately for the three elements f'_{xx}, f'_{xy} and f'_{xz}. The simplest situation occurs for the element f'_{xx}, which we will treat below. The elements f'_{xy} and f'_{xz} require a slightly more complex treatment. Because the final result is the same, we leave this treatment for the appendix. The appendix also considers the effect of the substrate, which we ignore for the moment.

Our derivation is based on the characteristics of the far-field radiation pattern of a radiating dipole (dipole amplitude p). In particular we use the fact that the far-field radiation is transverse

$$\vec{E}(\vec{r}) \propto -\sin\theta\, p\,\hat{\theta} \tag{20}$$

where θ is the angle between $\vec{r}$ and $\vec{p}$ and $\hat{\theta}$ is the corresponding unit vector [30]. This means that the dipole amplitude can be obtained from the electric field if one assumes that the viewing direction is known

$$p \propto E/\sin\theta \tag{21}$$

We begin by considering Fig. 3(a). Here a nanoantenna is illuminated by a test dipole oscillating parallel to the x axis. We will denote this dipole $p_{\text{test,x}}$. Because the test dipole is located far away from the nanoantenna (at position r_{far}), this situation is equivalent to illuminating the nanoantenna with an x-polarized plane wave. We consider the induced field at the location r_{vib} close to the nanoantenna (this is the location where the vibrational dipole will be placed later on). This field will generally contain an x, y and z component. However, we only focus on the x component for now. In terms of the Green's function of this system we can write for this electric field

$$E_x(r_{\text{vib}}) = G_{xx}(r_{\text{vib}}, r_{\text{far}})\,p_{\text{test,x}} \tag{22}$$

The situation in the absence of the nanoantenna can be described with a similar diagram, which is displayed in Fig. 3(b). This system is described by the Green's function $G^{(0)}$ and in terms of this Green's function we can write

$$E_x^{(0)}(r_{\text{vib}}) = G_{xx}^{(0)}(r_{\text{vib}}, r_{\text{far}})\,p_{\text{test,x}} \tag{23}$$

This shows that we can write for the field enhancement tensor element f_{xx}

$$f_{xx} = \frac{G_{xx}(r_{\text{vib}}, r_{\text{far}})}{G_{xx}^{(0)}(r_{\text{vib}}, r_{\text{far}})} \tag{24}$$

#262910 Received 8 Apr 2016; revised 24 May 2016; accepted 24 May 2016; published 26 May 2016

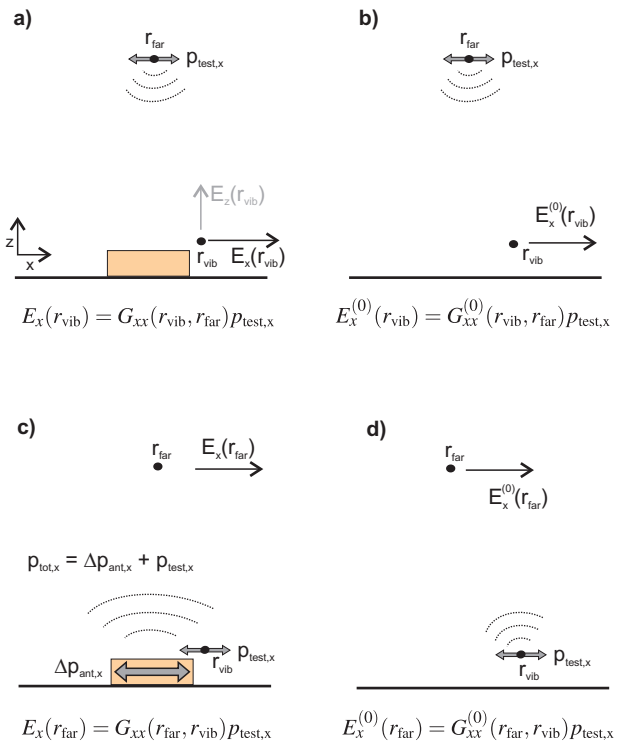

Fig. 3. Diagrams for computing the elements f_{xx} and f'_{xx}. In (a) and (b) a radiating test dipole is located at position r_{far} and the radiation pattern experienced by the nanoantenna resembles an x-polarized plane wave. In (c) and (d) the radiating test dipole is placed in the near field of the nanoantenna at position r_{vib}, so that it emulates a radiating vibrational dipole. Thin black arrows indicate electric fields while thick gray arrows indicate oscillating dipoles.

Next we focus on the dipole amplification factor f'_{xx}, for which we turn to Fig. 3(c) where we have placed the test dipole at the location r_{vib}. This dipole induces a dipole moment $\Delta\vec{p}_{ant}$ in the antenna (see Fig. 3(d)), and we are interested in its x component. Referring to Figs. 3(c) and 3(d) we write for the dipole amplification factor

$$f'_{xx} = \frac{p_{tot,x}}{p_{test,x}} \tag{25}$$

The aim is to obtain $p_{tot,x}$ from the far-field radiation pattern. The radiation pattern in Fig. 3(c) is the superposition of the radiation emitted by the nanoantenna ($\Delta p_{ant,x}$) and that of the test dipole $p_{test,x}$. However, for an observer located in the far-field this radiation pattern is equivalent to the radiation that would be emitted by a point-dipole with amplitude $p_{tot,x}$. As a consequence we can write

$$p_{tot,x} \propto E_x(r_{far}) \tag{26}$$

In similar manner we can obtain the amplitude of the test dipole in the absence of the nanoantenna (see Fig. 3) from the far-field

$$p_{test,x} \propto E_x^{(0)}(r_{far}) \tag{27}$$

#262910 Received 8 Apr 2016; revised 24 May 2016; accepted 24 May 2016; published 26 May 2016

In both cases we have assumed that the observation point is located directly above the dipole (i.e. $\theta = 0$). It is also important to realize that $p_{\mathrm{tot,y}}$ and $p_{\mathrm{tot,z}}$ do not necessarily vanish. However, they do not contribute to $E_{\mathrm{far,x}}$ because of the vectorial properties of the far-field dipole radiation. Again we rewrite these electric fields in terms of the Green's functions, which gives.

$$f'_{xx} = \frac{p_{\mathrm{tot,x}}}{p_{\mathrm{test,x}}} = \frac{E_x(r_{\mathrm{far}})}{E_x^{(0)}(r_{\mathrm{far}})} = \frac{G_{xx}(r_{\mathrm{far}}, r_{\mathrm{vib}})}{G_{xx}^{(0)}(r_{\mathrm{far}}, r_{\mathrm{vib}})} \tag{28}$$

Using the reciprocity relation we arrive at

$$f'_{xx} = f_{xx} \tag{29}$$

As is outlined in the appendix, it turns out that this equality remains valid in the presence of a substrate, and that similar equalities hold for the tensor elements f'_{yx} and f'_{zx}.

2.2.2. Expression for the cross-section change

Incorporating the results of the previous section we arrive at the following expression for the cross-section change of the nanoantenna

$$\Delta\sigma = \frac{2\pi S_{\mathrm{sub}}}{\lambda\varepsilon_0} \mathrm{Im}\left[\left((f_{xx}-1)^2 + f_{yx}^2 + f_{zx}^2\right)\alpha_{\mathrm{vib}}\right] \tag{30}$$

This expression holds for an antenna on a substrate. Equation (30) was derived for a nanoantenna interacting with a single vibrational dipole. However, because the expression is linear in α_{vib}, it can easily be generalized to the case of a nanoantenna interacting with many vibrations.

$$\Delta\sigma = \frac{2\pi N S_{\mathrm{sub}}}{\lambda\varepsilon_0} \mathrm{Im}\left[\overline{F_A^2}\alpha_{\mathrm{vib}}\right] \tag{31}$$

where N represents the number of vibrational dipoles and

$$\overline{F_A^2} = \frac{1}{V}\int_V \left((f_{xx}-1)^2 + f_{yx}^2 + f_{zx}^2\right) dV \tag{32}$$

represents the average nanoantenna amplification factor over the volume V where the vibrational dipoles are present. At first sight it may seem surprising that in the expression above there is an asymmetry between the appearance of the three tensor elements. We point out that this is merely a consequence of where we have truncated the perturbation expansion in Eq. (9). It turns out that the more symmetric expression

$$\overline{F_A^2} = \frac{1}{V}\int_V \left(f_{xx}^2 + f_{yx}^2 + f_{zx}^2\right) dV \tag{33}$$

corresponds to the sum of the four scattering diagrams displayed in Fig. 2. However, since it is convenient for the coming treatment, we will stick to a description based on a single scattering diagram and work with Eq. (32).

We are now in a position to compare the predictions of our analytical model with FDTD simulations. To this end we have simulated nanoantennas of varying length that are covered by a 10 nm layer of dielectric material. The antennas are simulated on top of a CaF_2 substrate ($n = 1.42$). The dielectric material is described by the following permittivity function that contains both a resonant and a non-resonant part

$$\varepsilon = \varepsilon_\infty + \varepsilon_{\mathrm{res}}(\omega) \tag{34}$$

#262910 Received 8 Apr 2016; revised 24 May 2016; accepted 24 May 2016; published 26 May 2016

where a Lorentz lineshape function is used for the resonant part

$$\varepsilon_{\mathrm{res}}(\omega) = \frac{\varepsilon_{\mathrm{lor}}\omega_0^2}{\omega_0^2 - \omega^2 - 2i\gamma\omega} \tag{35}$$

As a first step we consider a material that mimics the narrow-band absorption line of the carbonyl vibration of PMMA. We model this absorption band using a background permittivity ε_∞ of 1, a center frequency ω_0 of 1730 cm^{-1}, a FWHM (2γ) of 23 cm^{-1}, and an amplitude $\varepsilon_{\mathrm{lor}}$ of 0.015 (reproducing the experimentally observed absorption coefficient of the carbonyl band of PMMA). Using these permittivity parameters we performed FDTD simulations to obtain the nanoantenna-enhanced vibrational spectrum (Fig. 4, blue lines) for two representative nanoantennas. In order to use Eq. (31) we need to relate the permittivity to the vibrational polarizability, for which we employ the Clausius-Mossotti equation [30]

$$\rho\alpha_{\mathrm{vib}} = 3\varepsilon_0\left(\frac{\varepsilon - 1}{\varepsilon + 2}\right) \tag{36}$$

where ρ is the volume concentration of dipoles. Here we have arbitrarily assumed one dipole per FDTD simulation mesh cell ($\rho = 1/125$ nm^{-3}). In Fig. 4 we compare the antenna-enhanced vibrational spectrum as obtained from the FDTD simulations with a calculation based on Eq. (31). The amplification factor $\overline{F_a^2}$ needed for this calculation was obtained from the simulations of the uncoated antennas. As can be seen the agreement between the

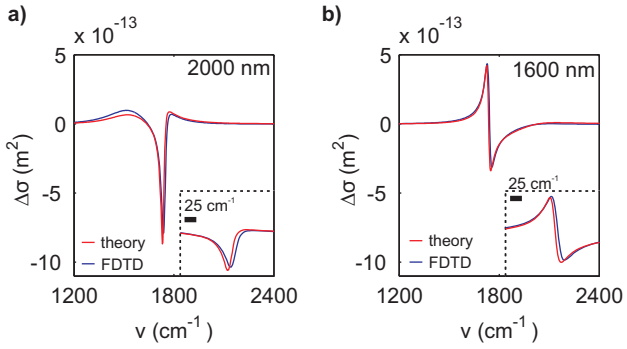

Fig. 4. Comparison of the analytical model (Eq. (31)) with FDTD simulations. The blue curves represent FDTD simulations (coated nanoantennas minus uncoated nanoantenna) and the red curves are computed using Eq. (31) where the nanoantenna amplification factor $\overline{F_A^2}$ was taken from the simulations of the uncoated nanoantennas. The permittivity of the dielectric was modeled as a Lorentzian band ($\varepsilon_{\mathrm{lor}} = 0.0149$, $\omega_0 = 1730$ cm^{-1}, $2\gamma = 23$ cm^{-1}) with a background permittivity ε_∞ of 1.

FDTD simulations and Eq. (31) is excellent except for a very small frequency shift of a few wavenumbers (see inset). Next it is interesting to see whether our model can explain the observed shift of the nanoantenna resonance (Fig. 1(c)) when the dielectric material on top of the nanoantenna is characterized by a frequency-independent index of refraction. To this end we describe the dielectric using the known index of refraction (n_∞) of PMMA of 1.48, i.e. $\varepsilon_\infty = n_\infty^2$ and $\varepsilon_{\mathrm{lor}} = 0$ [31]. Again we use the Clausius-Mossotti equation to obtain the polarizability from the permittivity. In Fig. 5 we compare the cross-section change from the FDTD simulation with the analytical model. Again we get a very good agreement between the analytical model and the simulations, except that the model overestimates the cross-section change by approximately

#262910 Received 8 Apr 2016; revised 24 May 2016; accepted 24 May 2016; published 26 May 2016

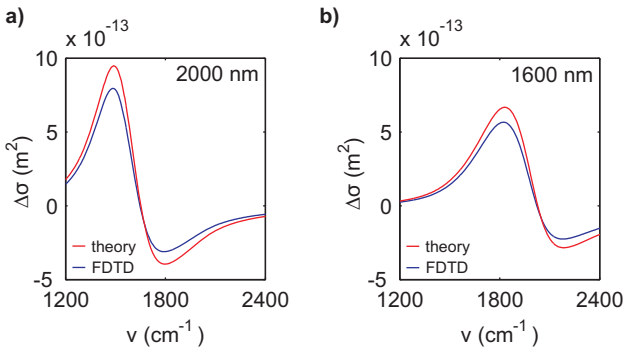

Fig. 5. Comparison of the analytical model (Eq. (31)) with FDTD simulations in the case of a dielectric represented by a frequency-independent refractive index of 1.48. The blue curves represent FDTD simulations (coated nanoantennas minus uncoated nanoantenna) and the red curves are computed using Eq. (31) where the nanoantenna amplification factor $\overline{F_A^2}$ was taken from the simulations of the uncoated nanoantennas.

20%. For both nanoantennas we observe an increased cross-section on the low-frequency side and a decreased cross-section on the high-frequency side, which is exactly the redshift illustrated in Fig. 1(c). It is worthwhile to point out that the nanoantenna redshift is a manifestation of the backaction of the molecular dipoles on the nanoantennas, just as in the case of dipoles characterized by a vibrational resonance. In addition, it is interesting to note that the observed cross-section change is directly proportional to the imaginary part of $\overline{F_A^2}$.

As a final consistency check we simulate the effect of a material which displays both a background index of refraction (n_∞) and an absorptive Lorentz term. In order to accurately mimic PMMA we choose $n_\infty = \sqrt{\varepsilon_\infty} = 1.48$ and $\varepsilon_{\text{lor}} = 0.022$. Together these two parameters match both the real and imaginary permittivity of PMMA in the carbonyl region [31]. In a similar manner as was done above we compare the results of the simulations with the analytical model (Fig. 6). Curiously we observe that the very good description we achieved

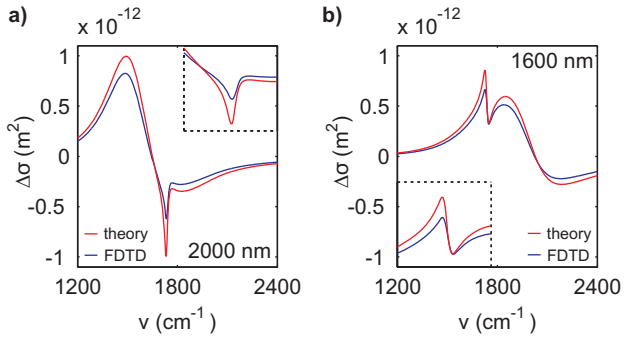

Fig. 6. Simulated (blue line) and calculated (red line) cross-section changes for nanoantennas coated with a dielectric material with a realistic model for the PMMA permittivity. The permittivity parameters used are $\varepsilon_{\text{lor}} = 0.022$, $\omega_0 = 1730$ cm^{-1}, $\gamma = 23$ cm^{-1} and $\varepsilon_\infty = n_\infty^2 = 2.19$.

when simulating a material with only a resonant permittivity or only an off-resonant permittivity

#262910 Received 8 Apr 2016; revised 24 May 2016; accepted 24 May 2016; published 26 May 2016

disappears when we simulate a realistic material which has both effects. As expected we see that the off-resonant part of the cross-section change is still overestimated by approximately 20%. However, surprisingly the resonant part of the cross-section change, which showed an almost perfect match in Fig. 4, is now overestimated by almost a factor of 2. This suggests that a crucial element is still missing in our analytical model. The fact that we obtain a good fit when choosing either $\varepsilon = \varepsilon_\infty$ or $\varepsilon = \varepsilon_{\mathrm{lor}}(\omega)$, but not when we describe ε as the sum of these contributions implies that there is an interaction effect between these different contributions to ε. Such interaction effect could arise if the interaction between different vibrational dipoles with each other is important. In the next section we will examine how this effect can be incorporated in our model.

2.3. Step 3: the Lorentz local field and the depolarization field

In order to treat the interactions between the vibrational dipoles we consider the electric field inside a piece of dielectric material that is irradiated by a homogeneous field E_0 (we assume the dimensions of the material are smaller than the wavelength of the light). A microscopic dipole inside the material experiences a field that differs from the externally applied field E_0. In fact, there are two additional contributions to the microscopic field. Firstly there is the Lorentz local field (LLF)

$$E_{\mathrm{LLF}} = \frac{P}{3\varepsilon_0} \tag{37}$$

which points in the same direction as the external field (P is the polarization of the material, i.e. dipole moment per unit volume) [30]. The Lorentz local field accounts for the difference between the macroscopically averaged field applied to a sample and the microscopic field experienced inside the sample. The second field that needs to be considered is the so-called depolarization field due the accumulation of charges on the boundaries of the material. The depolarization field E_{depol} points opposite to the externally applied field E_0. In Fig. 7 we have schematically illustrated these fields for a dielectric particle. The reason we have chosen to

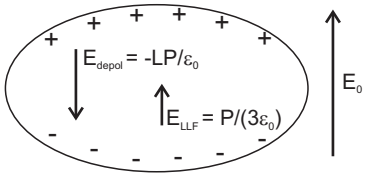

Fig. 7. Schematic representation of the different electric fields that need to be considered when computing the polarizability of an ellipsoidal particle. Here we have drawn an oblate ellipsoid, for which the depolarization factor is approximately 0.5.

illustrate these effects for an ellipsoidal particle is that for this particular shape the induced polarization is independent of the position inside the particle leading to the simple analytical expression for the depolarization field

$$E_{\mathrm{depol}} = -L\frac{P}{\varepsilon_0} \tag{38}$$

where L is the so-called depolarization factor (a dimensionless parameter between 0 and 1), which depends on the shape of the ellipsoid [23]. According to the reasoning above the field experienced by a microscopic dipole moment inside the material is

$$E = E_0 - L\frac{P}{\varepsilon_0} + \frac{P}{3\varepsilon_0} \tag{39}$$

#262910 Received 8 Apr 2016; revised 24 May 2016; accepted 24 May 2016; published 26 May 2016

Using $P = \rho\alpha E$ one can solve for the microscopic field

$$E = F_M E_0 \tag{40}$$

and it becomes clear that the microscopic field is simply related to the external field by a scaling factor, which we will call the *molecular* field-enhancement factor

$$F_M = \frac{1}{1+\rho\alpha/\varepsilon_0(L-1/3)} \tag{41}$$

$$= \frac{(\varepsilon+2)/3}{L(\varepsilon-1)+1} \tag{42}$$

In the second line we have used the Clausius-Mossotti equation to relate α and ε. We should point out that, strictly speaking, Eq. (40) only holds for an ellipsoidal particle that is illuminated by a homogeneous field E_0. This is quite different from our situation, in which we have a shell of PMMA that is excited by the inhomogeneous near field of the nanoantenna. Nevertheless we will make the *assumption* that Eq. (40) still holds in our case. This implies that the field experienced by the vibrational dipoles is scaled by the factor F_M compared to the antenna near field. Using the same reciprocity argument as in the previous section this also means that the field radiating back on the nanoantenna is scaled by the same factor compared to the field in the absence of local-field effects. This leads to the following expression for the cross-section change of the nanoantenna due to the PMMA shell

$$\Delta\sigma = \frac{2\pi N S_{\text{sub}}}{\lambda\varepsilon_0}\,\text{Im}\left[\overline{F_A^2}F_M^2\alpha_{\text{vib}}\right] \tag{43}$$

Let us now compare the prediction of this new expression, which contains one free parameter (the depolarization factor L), with the FDTD simulations. Figure 8 shows the simulations of the cross-section changes of two nanoantennas that are covered with a dielectric material that displays both a background permittivity and a resonant permittivity. In total we have simulated 8 nanoantennas with lengths between 1400 nm and 2600 nm, and we obtain an excellent fit of the analytic model if we choose a depolarization factor $L = 0.49$. It is important to point out

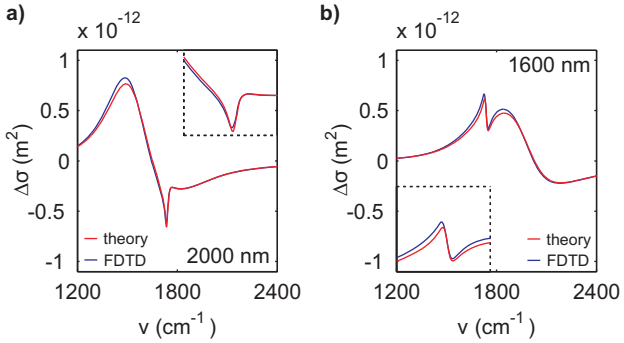

Fig. 8. Simulated (blue line) and calculated (red line) cross-section changes for nanoantennas coated with a dielectric material with a realistic model for the PMMA permittivity. The calculations were done on the basis of Eq. (43) using a depolarization factor L of 0.49. The permittivity parameters used are $\varepsilon_{\text{lor}} = 0.022$, $\omega_0 = 1730$ cm^{-1}, $\gamma = 23$ cm^{-1} and $\varepsilon_\infty = n_\infty^2 = 2.19$.

that the excellent fit observed in Fig. 8 is not simply the result of a fortuitous scaling of α_{vib} by

#262910 Received 8 Apr 2016; revised 24 May 2016; accepted 24 May 2016; published 26 May 2016

F_M^2 (see Eq. (43)). This can be seen by comparing Figs. 6 and 8, which shows that F_M^2 scales the resonant and non-resonant parts of the cross-section change by different amounts.

To gain more insight into the role of the molecular field enhancement F_M it is useful to explicitly consider its functional dependence, which we have plotted in Fig. 9. For comparison this figure also displays a plot of α_{vib}. We see that, similar to α_{vib}, F_M^2 contains a resonant and

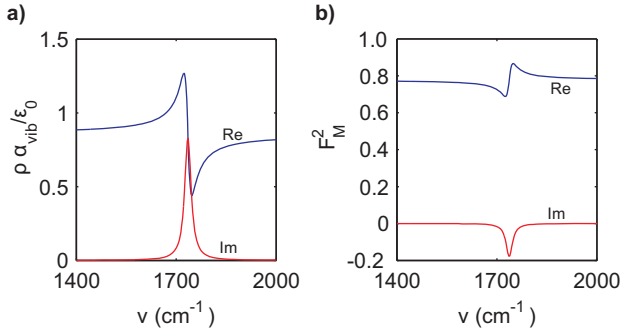

Fig. 9. a) Plot of the vibrational polarizability of PMMA that follows from the experimental permittivity. b) Plot of the factor F_M^2 assuming the experimental polarizability of PMMA and a depolarization factor L of 0.49.

a non-resonant contribution, so that we can write these quantities as follows

$$\alpha_{\text{vib}}(\omega) = \alpha_{\text{res}}(\omega) + \alpha_\infty \tag{44}$$

$$F_M^2(\omega) = (F_M^2)_{\text{res}}(\omega) + (F_M^2)_\infty \tag{45}$$

To excellent approximation the resonant contribution of F_M^2 is Lorentzian, but contrary to the resonant contribution of α_{vib} it has a negative amplitude. It is insightful to perform a similar separation into a resonant and non-resonant contribution for the amplified vibrational spectrum $\Delta\sigma$. The non-resonant contribution has the following form

$$\Delta\sigma_{\text{non-res}} = \frac{2\pi N S_{\text{sub}}}{\lambda \varepsilon_0} \text{Im}\left[\overline{F_A^2}(F_M^2)_\infty \alpha_\infty\right] \tag{46}$$

which immediately shows that the molecular field simply scales the cross-section change by the factor $(F_M^2)_\infty$. Next we consider the resonant part of the cross-section change, which can be identified with the cross terms between the resonant and non-resonant parts of (F_M^2) and α_{vib},

$$\Delta\sigma_{\text{res}} = \frac{2\pi N S_{\text{sub}}}{\lambda \varepsilon_0} \text{Im}\left[\overline{F_A^2}\left[(F_M^2)_\infty \alpha_{\text{res}} + \alpha_\infty (F_M^2)_{\text{res}}\right]\right] \tag{47}$$

Here we neglected the contribution of the term proportional to $\alpha_{\text{res}}(F_M^2)_{\text{res}}$. It now becomes clear why neglecting the local field effects had led to such a great overestimation of the resonant cross-section change in Fig. 6. The point is that $\Delta\sigma_{\text{res}}$ is made up of two opposing contributions, of which one owes its resonant character to the resonance in α_{vib} while the second owes its resonant character to the resonance in F_M^2. The former contribution corresponds to the signal we had already derived in the previous section (except for the fact that it is now scaled down by the factor $(F_M^2)_\infty$). The latter contribution, however, was missed in our previous analysis. Thus we see that the molecular field decreases the amplification of the vibrational spectrum by the nanoantenna. Let us next quantify this effect. To this end we note that α_{vib} and F_M have the

#262910 Received 8 Apr 2016; revised 24 May 2016; accepted 24 May 2016; published 26 May 2016

same functional form, which to first order in $\varepsilon_{\text{res}}(\omega)$ can be approximated as follows.

$$\frac{a+c\varepsilon_{\text{res}}(\omega)}{c+d\varepsilon_{\text{res}}(\omega)} \approx \frac{a}{c}+\frac{a}{c}\left(\frac{b}{a}-\frac{d}{c}\right)\varepsilon_{\text{res}}(\omega) \tag{48}$$

Using this approximation it is a simple matter to find the following expressions for $\Delta\sigma_{\text{res}}$ and $\Delta\sigma_{\text{non-res}}$

$$\Delta\sigma_{\text{non-res}}(\omega) = \frac{2\pi N S_{\text{sub}} S_{\text{nr}}}{\lambda\varepsilon_0}\text{Im}\left[\overline{F_A^2}(\omega)\right] \tag{49}$$

$$\Delta\sigma_{\text{res}}(\omega) = \frac{2\pi N S_{\text{sub}} S_{\text{r}}}{\lambda\varepsilon_0}\text{Im}\left[\overline{F_A^2}(\omega)\varepsilon_{\text{res}}(\omega)\right] \tag{50}$$

where the scaling factors for the resonant and non-resonant signals have been defined as

$$S_{\text{nr}} = \frac{(\varepsilon_\infty+2)(\varepsilon_\infty-1)}{3(L(\varepsilon_\infty-1)+1)^2} \tag{51}$$

$$S_{\text{r}} = \frac{(2/3-L)(\varepsilon_\infty-1)+1}{(L(\varepsilon_\infty-1)+1)^3} \tag{52}$$

As expected we see that the resonant and non-resonant part of the cross-section show a different scaling behavior as a function of the background permittivity. As a final check of the validity of our treatment we compare the obtained analytical expressions for the scaling factors S_r and S_{nr} with the results of simulations. These results are shown in Fig. 10. The data points in this figure represent the amplitudes of the resonant and non-resonant cross-section changes of a coated 2000 nm nanoantenna, where we have used the same permittivity function $\varepsilon(\omega)$ as in Fig. 8 except that we have varied the background permittivity ε_∞. In order to separately obtain $\Delta\sigma_{\text{res}}(\omega)$ and $\Delta\sigma_{\text{non-res}}(\omega)$ from our simulations we performed two simulations for every value of ε_∞: one with $\varepsilon(\omega)=\varepsilon_\infty+\varepsilon_{\text{res}}(\omega)$ and the other with $\varepsilon(\omega)=\varepsilon_\infty$. The theoretical curves (Eq. (51)-(52)) were calculated using the previously determined value of 0.49 for the depolarization factor L. As can be seen we obtain an excellent agreement between the theory and the simulations. For reference we have plotted two additional curves in these graphs. The first (purple line) represents the signal that one obtains if one completely ignores all local-field effects; that is, when ignoring both the factor F_M^2 and the Lorentz local field factor in the Clausius-Mossottti equation (meaning that we use $\rho\alpha_{\text{vib}}=\varepsilon_0(\varepsilon-1)$). The second graph represents the signal one obtains upon inclusion of the Lorentz local field factor in the Clausius-Mossotti equation but without the factor F_M^2. We see that the local field effects drastically decrease the visibility of the vibrational amplification by the nanoantenna.

At this point it is instructive to briefly summarize the different screening effects that we have identified. We have seen that the *maximum* degree of amplification is determined by the square of the nanoantenna field enhancement ($\overline{F_A^2}$). This maximum amplification factor is identical for the resonant ($\Delta\sigma_{\text{res}}$) and non-resonant signals ($\Delta\sigma_{\text{non-res}}$). There are two effects that decrease this maximum amplification. Firstly, the amplification is weakened by the effect of the substrate through the parameter S_{sub} (for both the resonant and the non-resonant signals). Secondly, the amplification is further decreased due to the local-field effect (through the screening parameters S_{r} and S_{nr}). Interestingly it turns out that the local-field effect is fully mediated by the background refractive index n_∞ of the material being sensed. This can be seen from the fact that for $n_\infty=1$, the amplitude of the amplified signal is independent of whether local-field effects are included or not. We also see the that the local field has a larger effect on the resonant signal compared to the non-resonant signal. For instance, up to a refractive index of approximately 1.5 the non-resonant signal is hardly affected by the local-field effects while the

#262910 Received 8 Apr 2016; revised 24 May 2016; accepted 24 May 2016; published 26 May 2016

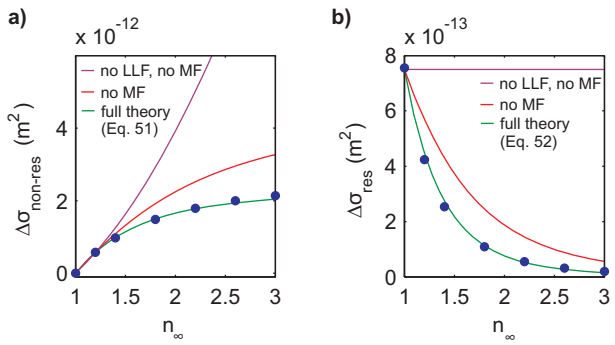

Fig. 10. Amplitude of the non-resonant (a) and resonant (b) cross-section change as a function of the background refractive index $n_\infty = \sqrt{\varepsilon_\infty}$ of the coating material. The data points represent the maximum of the simulated cross-section change (which lies at 1420 cm^{-1} for the non-resonant signal and 1730 cm^{-1} for the resonant signal). The simulations were carried out for a 2000 nm nanoantenna coated with a 10 nm layer of dielectric material characterized by the permittivity from Eq. (34) with $\varepsilon_{\text{lor}} = 0.022$, $\omega_0 = 1730$ cm^{-1} and $2\gamma = 23$ cm^{-1}. The green curves represent calculations based on Eqs. (51) and (52) with $L = 0.49$. The red curves represent calculations when the molecular field (MF) enhancement is neglected (i.e. $F_M^2 = 1$). The magenta curves represent calculations where, in addition, the Lorentz local field (LLF) factor in the Clausius-Mossotti equation is ignored (i.e. $\rho\alpha_{\text{vib}} = \varepsilon_0(\varepsilon - 1)$).

resonant signal already shows a marked decrease. From a sensing perspective the result shown in Fig. 10 implies that vibrations which lie in a spectral region with a low refractive index can be detected most efficiently. For example, an increase in the refractive index from 1.5 to 2 leads to a decrease of the amplified vibrational signal by a factor of ~ 3. For completeness we mention that another important factor determining the vibrational amplification is the orientation of the transition dipole moment of a vibration with respect to the local electric field (that is, vibrations with a transition dipole moment perpendicular to the local electric field are not amplified). As this effect is well documented in the literature [2], we have not included it in our present treatment although it can be done straightforwardly.

We return to the depolarization factor and the value of 0.49, which has been found to accurately describe our data. The question arises as to how this value should be interpreted. In our treatment we have implicitly assumed that the depolarization factor is independent of the location inside the dielectric material. Strictly speaking this assumption is only correct for ellipsoidal particles. The fact that we nevertheless obtain an excellent description of our signals suggests that, although the polarization and depolarization fields are not homogeneous over the PMMA shell, the proportionality relation between these two quantities (as expressed by Eq. (38)) remains valid to a good approximation. To interpret the magnitude of L it is useful to consider how L depends on the shape of an ellipsoidal particle. It is well known that spherical particles are characterized by $L = 1/3$ and that L decreases to a value of 0 as the particles become prolate (for an electric field polarized parallel to the long axis). For flatter particles, i.e. oblate ellipsoids, the opposite occurs and L increases up to its limiting value of 1 (for an electric field polarized parallel to the short axis). Apparently, the flatter the particle is, the better the external electric field can be shielded by the depolarization field. The value of $L = 0.49$, which corresponds to an oblate ellipsoid with a shape similar to the one drawn in Fig. 7 (that is, with a short axis approximately half the length of the long axis), indicates a rather good shielding of the nanoantenna field by the PMMA. This is probably a consequence of the fact

#262910 Received 8 Apr 2016; revised 24 May 2016; accepted 24 May 2016; published 26 May 2016

that for the entire PMMA shell the near field of the nanoantenna is perpendicular to the surface of the PMMA. With respect to the nanoantenna near field the PMMA shell therefore acts as a flat particle.

We have seen that for the nanoantenna geometry described in this work the local-field effects tend to decrease the plasmonic enhancement of a vibrational resonance ($S_r < 1$; see Fig. 10(b)). Now the interesting question arises as to whether it would be possible to design a nanoantenna whose plasmonic enhancement is actually boosted by the local fields rather than weakened. From Eq. (52) it can easily be seen that decreasing the depolarization factor L leads to an increase of S_r thereby increasing the plasmonic enhancement. It turns out that for $L < 0.1$ the resonant scaling factor S_r can even attain values that are larger than unity over the entire refractive index range displayed in Fig. 10. For instance, if one could achieve a vanishing depolarization factor ($L = 0$), then for a vibrational mode with a typical background refractive index n_∞ of 1.65 one would obtain a plasmonic enhancement that is 10 times larger compared to the enhancement obtained with the present geometry ($L = 0.49$). A depolarization factor of zero corresponds to the case in which the depolarization field effectively vanishes over the volume of the sensed material. This situation occurs naturally for strongly prolate particles (with the electric field polarized along the long axis). Alternatively one could imagine achieving this condition through a nanoantenna geometry in which the sensed material is not applied homogeneously over the entire nanoantenna, but rather as nanostructured patches, designed in such a way to cause the depolarization field to effectively vanish over the material. These considerations demonstrate that engineering of the local molecular field could potentially yield a novel strategy to significantly boost the amplification of vibrational signals by infrared nanoantennas.

3. Conclusion

We have presented a model which describes the interaction between molecular vibrations and infrared nanoantennas. The model allows one to quantitatively compute the cross-section change displayed by an infrared nanoantenna when it is covered by a thin layer of dielectric material. Our treatment is based on a perturbation expansion in which the total cross-section change of the nanoantenna is split up into a series of contributions from (virtual) interaction processes, each of which has a straightforward physical interpretation. The model demonstrates that the main contribution to the cross-section change is due to a backaction process: the nanoantenna near field excites the molecular vibrations, which in turn radiate back onto the nanoantenna. This backaction process explains both the lineshape of the amplified vibrational signal and its amplitude. The lineshape is determined by the phase lag between the incident radiation and the reradiated field. Depending on the detuning between the nanoantenna and the molecular vibrations, this phase lag can have any value between 0 and 2π, which explains the variety of observed lineshapes ranging from absorptive peaks and dips to fully dispersive shapes. The plasmonic enhancement of the vibrational signal is firstly determined by the square of the field enhancement of the nanoantenna. In addition, however, it turns out that the local molecular field plays an important role as it effectively scales the nanoantenna near field. Interestingly, depending on the exact circumstances, this local-field effect can either decrease or further boost the plasmonic enhancement by the nanoantenna. This could provide an avenue for achieving particularly strong plasmonic enhancements by rationally engineering the local field.

Appendix A: simulation details

The finite-difference time-domain simulation were performed using a commercially available software package (Lumerical). We used a total-field-scattered-field (TFSF) source to compute

#262910 Received 8 Apr 2016; revised 24 May 2016; accepted 24 May 2016; published 26 May 2016

the extinction cross section of 8 nanoantennas of varying lengths (between 1400 nm and 2600 nm). The antennas were simulated on top of a CaF_2 substrate ($n = 1.42$). The optical constants of gold were taken from Palik [32]. We computed the extinction for both the bare antennas and for antennas covered with a 10 nm layer of PMMA on each face. We examined a number of different permittivity functions for the PMMA, as described in the main text. For both the antennas and the PMMA a mesh of 5 nm was used. Because of the sharp PMMA resonance, relatively long simulation times of 2000 fs were required whenever this resonance was included in the permittivity function.

Appendix B: derivations

In this appendix we provide the derivation proving that $f'_{xy} = f_{xy}$ and $f'_{xz} = f_{xz}$. In the second part we demonstrate that these equalities remain valid for a dipole on a surface.

3.1. The element f'_{xy}

The element f'_{xy} can be obtained via a slightly modified approach compared to the one discussed in the main text. The diagrams required are shown in Fig. 11. Using the diagrams in Figs. 11(a) and 11(b) we write for the field-enhancement tensor

$$f_{yx} = \frac{G_{yx}(r_{\mathrm{vib}}, r_{\mathrm{far}})}{G^{(0)}_{xx}(r_{\mathrm{vib}}, r_{\mathrm{far}})} \tag{53}$$

Next from Figs. 11(c) and 11(d) we find that

$$f'_{xy} = \frac{\Delta p_{\mathrm{ant,x}}}{p_{\mathrm{test,y}}} = \frac{E_x(r_{\mathrm{far}})}{E^{(0)}_y(r_{\mathrm{far}})} \tag{54}$$

$$= \frac{G_{xy}(r_{\mathrm{far}}, r_{\mathrm{vib}})}{G^{(0)}_{yy}(r_{\mathrm{far}}, r_{\mathrm{vib}})} \tag{55}$$

In writing the first line we have used the fact that $E_x(r_{\mathrm{far}})$ reports only on $p_{\mathrm{ant,x}}$ even though $p_{\mathrm{ant,y}}$ and $p_{\mathrm{ant,z}}$ are non-vanishing. Because of symmetry

$$G^{(0)}_{yy}(r_{\mathrm{far}}, r_{\mathrm{vib}}) = G^{(0)}_{xx}(r_{\mathrm{far}}, r_{\mathrm{vib}}) \tag{56}$$

from which follows that

$$f'_{xy} = f_{yx} \tag{57}$$

3.2. The element f'_{xz}

The element f'_{xz} is somewhat more difficult to evaluate. Here we need to consider a test dipole that is oriented along the z axis. However, the amplitude of this dipole cannot be obtained form the field at r_{far} as the radiated field vanishes in the direction parallel to the dipole moment. Because of this we will adopt a slightly different strategy in which we place the observation point r_{far} such that the dipoles are observed under a slight angle θ. We will define a second coordinate system with axes z' and x' (see Fig. 12(a)). We can define the following field enhancement tensor element (applying to non-normal incidence)

$$f_{zx}[\theta] = \frac{E_z(r_{\mathrm{vib}})}{E^{(0)}_x(r_{\mathrm{vib}})} \tag{58}$$

$$= \frac{G_{zx'}(r_{\mathrm{vib}}, r_{\mathrm{far},\theta})}{G^{(0)}_{xx'}(r_{\mathrm{vib}}, r_{\mathrm{far},\theta})} \tag{59}$$

#262910 Received 8 Apr 2016; revised 24 May 2016; accepted 24 May 2016; published 26 May 2016

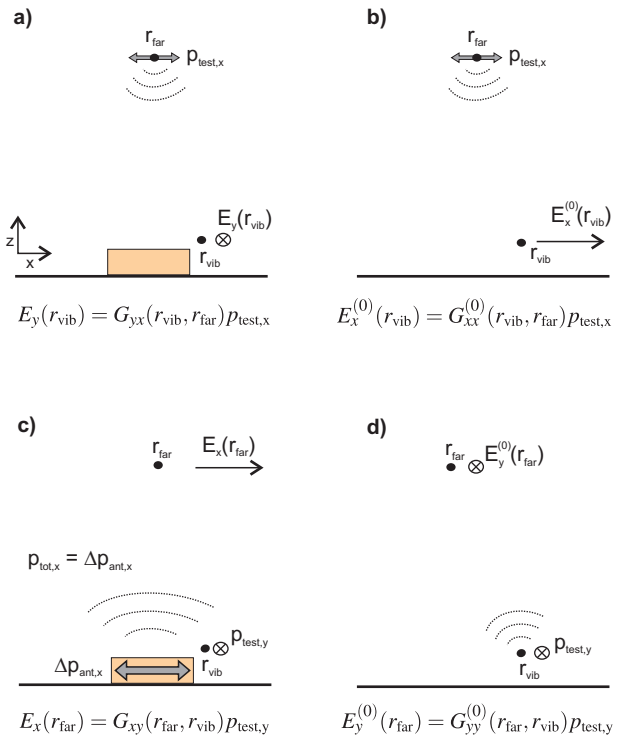

Fig. 11. Diagrams for computing the element f'_{xy}. In these diagrams the far-field source is placed in such a way that the nanoantenna is illuminated under a slight angle θ. We have defined a secondary coordinate system with the z' axis parallel to the k vector of the illumination; the x' axis is perpendicular to this direction and parallel to the electric field of the source dipole.

which obviously tends to f_{zx} (which is the element that appears in Eq. (19)) as θ approaches zero.

Now a difficulty occurs when we attempt to obtain the dipole moment $p_{\text{ant,x}}$ from the field $E_{\text{far},x'}$. The point is that this field does not only depend on $p_{\text{ant,x}}$ but also on $p_{\text{ant,z}}$. However, if the angle θ is small then

$$p_{\text{ant,x}} \propto E_{x'}(r_{\text{far},\theta})/\sin(\pi/2-\theta) = E_{x'}(r_{\text{far},\theta})/\cos(\theta) \tag{60}$$

is a good approximation, which becomes exact in the limit $\theta \to 0$. From Fig. 12(d) it follows that

$$p_{\text{test,z}} \propto E^{(0)}_{x'}(r_{\text{far},\theta})/\sin(\theta) \tag{61}$$

From these two expressions we can obtain

$$f'_{xz}[\theta] = \frac{\Delta p_{\text{ant,x}}}{p_{\text{test,z}}} \tag{62}$$

$$= \frac{E_{x'}(r_{\text{far},\theta})}{E^{(0)}_{x'}(r_{\text{far},\theta})/\tan\theta} \tag{63}$$

$$= \frac{G_{x'z}(r_{\text{far},\theta}, r_{\text{vib}})}{G^{(0)}_{x'z}(r_{\text{far},\theta}, r_{\text{vib}})/\tan\theta} \tag{64}$$

#262910 Received 8 Apr 2016; revised 24 May 2016; accepted 24 May 2016; published 26 May 2016

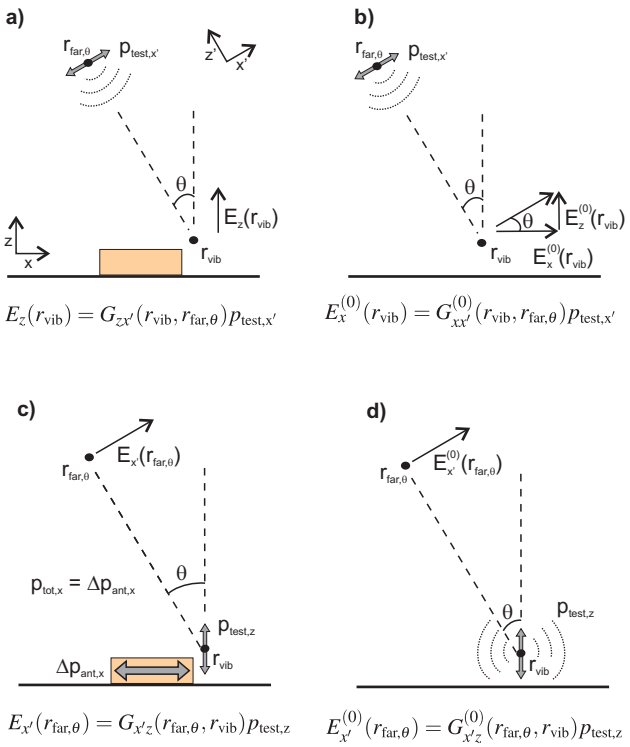

Fig. 12. Diagrams for computing the element f'_{xz}. In these diagrams the far-field source is placed in such a way that the nanoantenna is illuminated under a slight angle θ. We have defined a secondary coordinate system with the z' axis parallel to the k vector of the illumination; the x' axis is perpendicular to this direction and parallel to the electric field of the source dipole.

Here the parameter θ refers to the fact that the tensor element $f'_{xz}[\theta]$ (which itself does not depend on θ) is evaluated using the observation point $r_{far,\theta}$. Using the reciprocity relation we rewrite this into

$$f'_{xz}[\theta] = \frac{G_{zx'}(r_{vib}, r_{far,\theta})}{G^{(0)}_{zx'}(r_{vib}, r_{far,\theta})/\tan\theta} \tag{65}$$

$$= \frac{G_{zx'}(r_{vib}, r_{far,\theta})}{G^{(0)}_{xx'}(r_{vib}, r_{far,\theta})} \tag{66}$$

$$= f_{zx}[\theta] \tag{67}$$

where the second step follows from Fig. 12(b). In the limit $\theta \to 0$ we obtain

$$f'_{xz} = f_{zx} \tag{68}$$

3.3. Effect of the substrate

The derivations above have relied strongly on the properties of the dipole radiation field. The question now arises whether this derivation still holds for a dipole located above a substrate (given the fact that the substrate modifies the dipolar radiation field). Fortunately in our case

#262910 Received 8 Apr 2016; revised 24 May 2016; accepted 24 May 2016; published 26 May 2016

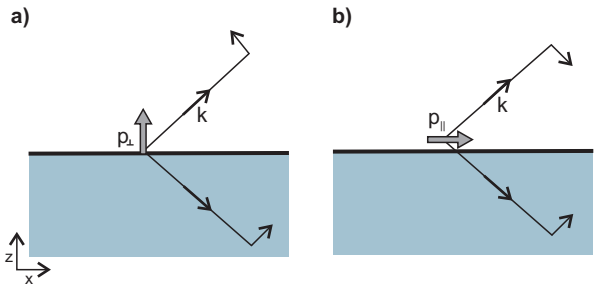

Fig. 13. Diagrams for evaluating the radiation pattern of out-of-plane (a) and in-plane dipoles that are located above a substrate. We assume that the distance above the substrate is much smaller than the wavelength.

the situation is relatively simple. We only need to consider the radiation pattern in the xz plane, and we need to do this for two cases: a dipole aligned along the z axis and a dipole aligned along the x axis. The radiation pattern in the upper plane is the superposition of the field emitted in the upward direction and the field reflected by the substrate. To obtain the far-field radiation patterns for the dipoles shown in Figs. 13(a) and 13(b) we simply reflect the downward traveling ray and scale it by the Fresnel reflection coefficient. The validity of this approach follows from the fact that in the far-field the radiation pattern of a dipole is given by its angular spectrum [26]; the rays in Fig. 13 should be interpreted as the plane-wave components that form the angular spectrum representation of the dipole radiation field. Taking into account the direction of the different electric field vectors we see that this leads to different radiation patterns for parallel and perpendicular pointing dipoles.

$$E \propto (1+r_\theta)\sin\theta\, p_\perp \tag{69}$$

$$E \propto (1-r_\theta)\cos\theta\, p_{||} \tag{70}$$

Here r_θ is the Fresnel reflection coefficient for a p-polarized plane wave incident at an angle θ. Now it becomes clear that in the evaluation of f'_{xx} and f'_{xy} this effect has no influence as in these cases we only compare in-plane dipoles with each other (see Figs. 3(c) and 3(d) and Figs. 11(c) and 11(d)). For the evaluation of f'_{xz} this is not the case, however. That is because there we compare an in-plane dipole with an out-of-plane dipole (Figs. 12(c) and 12(d)), and Eq. (65) therefore modifies into

$$f'_{xz}[\theta] = \frac{1+r_\theta}{1-r_\theta}\frac{E_{x'}(r_{\mathrm{far},\theta})}{E^{(0)}_{x'}(r_{\mathrm{far},\theta})/\tan\theta} \tag{71}$$

$$= \frac{1+r_\theta}{1-r_\theta}\frac{G_{x'z}(r_{\mathrm{far},\theta},r_{\mathrm{vib}})}{G^{(0)}_{x'z}(r_{\mathrm{far},\theta},r_{\mathrm{vib}})/\tan\theta} \tag{72}$$

At first sight it seems that this expression implies that Eq. (68) no longer holds. However, one should consider that in the presence of a substrate (see Fig. 12(b))

$$E^{(0)}_z(r_{\mathrm{vib}}) \neq \tan\theta E^{(0)}_x(r_{\mathrm{vib}}) \tag{73}$$

In fact, the Fresnel reflection of the incoming plane wave leads to

$$E^{(0)}_x(r_{\mathrm{vib}}) = (1-r_\theta)\cos\theta\, E_0 \tag{74}$$

$$E^{(0)}_z(r_{\mathrm{vib}}) = (1+r_\theta)\sin\theta\, E_0 \tag{75}$$

#262910 Received 8 Apr 2016; revised 24 May 2016; accepted 24 May 2016; published 26 May 2016

and as a consquence

$$G^{(0)}_{zx'}(r_{\mathrm{vib}}, r_{\mathrm{far},\theta}) = \tan\theta \frac{1+r_\theta}{1-r_\theta} G^{(0)}_{xx'}(r_{\mathrm{vib}}, r_{\mathrm{far},\theta}) \tag{76}$$

Therefore we again end up with

$$f'_{xz} = f_{zx} \tag{77}$$

Acknowledgments

This work is part of the research program of the "Stichting voor Fundamenteel Onderzoek der Materie (FOM)", which is financially supported by the "Nederlandse organisatie voor Wetenschappelijk Onderzoek (NWO)". The authors thank Huib Bakker, Kobus Kuipers and Femius Koenderink for valuable discussions and Albert Polman for help with and access to the simulation software.

#262910 Received 8 Apr 2016; revised 24 May 2016; accepted 24 May 2016; published 26 May 2016